Liquid-gas phase transition in nuclei in the relativistic Thomas-Fermi theory

Tapas Sil,[1,*] B. K. Agrawal,[2,†] J. N. De,[1,‡] and S. K. Samaddar[2,§]
[1]*Variable Energy Cyclotron Centre, 1/AF Bidhannagar, Calcutta 700 064, India*
[2]*Saha Institute of Nuclear Physics, 1/AF Bidhannagar, Calcutta 700 064, India*
(Received 2 May 2000; published 9 April 2001)

The equation of state (EOS) of finite nuclei is constructed in the relativistic Thomas-Fermi theory using the nonlinear σ-ω-ρ model. The caloric curves are calculated by confining the nuclei in the freeze-out volume taken to be a sphere of size about 4–8 times the normal nuclear volume. The results obtained from the relativistic theory are not significantly different from those obtained earlier in a nonrelativistic framework. The nature of the EOS and the peaked structure of the specific heat C_v obtained from the caloric curves show clear signals of a liquid-gas phase transition in finite nuclei. The temperature evolution of the Gibbs potential and the entropy at constant pressure indicate that the characteristics of the transition are not too different from the first-order one.

DOI: 10.1103/PhysRevC.63.054604 PACS number(s): 25.70.Pq, 21.10.−k, 21.60.−n, 21.65.+f

I. INTRODUCTION

Nuclear caloric curves have been obtained from a number of experiments in recent times from energetic nucleus-nucleus collisions. In the GSI data [1] for Au+Au at 600*A* MeV, the temperature was found to be practically constant at a value of $T\sim 5$ MeV over the excitation energy (ϵ^*) range of 3–10 MeV per nucleon, after which ϵ^* was found to increase linearly with temperature as in a classical gas. This is suggestive of a sharp liquid-gas type phase transition. The caloric curve obtained from the collision of Au on C at 1*A* GeV in the EOS Collaboration experiment [2] also shows a plateau at $T\sim 6$ MeV; this is not as prominent as in the earlier case. However, the heat capacity C_v derived from this caloric curve of the EOS group shows a peaked structure at $T\sim 6$ MeV, indicating existence of a phase transition. Even at a relatively low bombarding energy of 47*A* MeV [3] for several reactions, it has been seen recently that the caloric curves show plateau at $T\sim 7$ MeV in the excitation energy range of $\sim$3.5–7 MeV per nucleon. It would be interesting to know whether this is a precursor to the liquid-gas phase transition in the finite nuclei. Theoretical analysis of infinite nuclear matter (symmetric as well as asymmetric), both in the nonrelativistic [4,5] and relativistic frameworks [6,7], predicts van der Waals–type isotherms in their equation of state (EOS), implying the coexistence of liquid and gas phases. Finite size effects and the Coulomb interaction between protons might change such a behavior, but the EOS of realistic nuclei, calculated only recently [8] in the nonrelativistic Thomas-Fermi (TF) theory, display the same kind of isotherms, liquid-gas coexistence, and a liquid-gas phase transition at a temperature quite below the critical temperature for infinite nuclear matter. The calculated transition temperatures are still somewhat higher than the observed ones, and the caloric curves do not match exactly the ones derived from experiments, but the calculations in Ref. [9] give unmistakable signals of the liquid-gas phase transition in finite size nuclear systems.

Relativistic mean field (RMF) theories have been applied successfully to explain the ground state properties of nuclei over the entire periodic table [10]. This theory has also proved to be very fruitful in explaining various details of exotic nuclei near the drip lines [11,12]. In contrast to the nonrelativistic models, the RMF theory uses a single set of parameters to explain all these properties. It would therefore be very interesting to investigate the EOS of finite nuclei and the related exotic phenomena like the liquid-gas phase transition in the relativistic approach. The present paper aims at understanding these thermodynamic properties of hot nuclei in a relativistic Thomas-Fermi (RTF) theory.

In Sec. II, we briefly outline the formalism used. The results and discussions are presented in Sec. III. The summary and conclusions are given in Sec. IV.

II. FORMALISM

A brief outline of the calculations of the relevant thermodynamic quantities in the relativistic Thomas-Fermi approximation is presented in this section. The Lagrangian density used is given by [10]

$$\begin{aligned}\mathcal{L}=&\bar{\Psi}_i(i\gamma^\mu\partial_\mu-M)\Psi_i+\frac{1}{2}\partial^\mu\sigma\partial_\mu\sigma-U(\sigma)-g_\sigma\bar{\Psi}_i\sigma\Psi_i\\&-\frac{1}{4}\Omega^{\mu\nu}\Omega_{\mu\nu}+\frac{1}{2}m_\omega^2\omega^\mu\omega_\mu-g_\omega\bar{\Psi}_i\gamma^\mu\omega_\mu\Psi_i\\&-\frac{1}{4}\vec{R}^{\mu\nu}\vec{R}_{\mu\nu}+\frac{1}{2}m_\rho^2\vec{\rho}^\mu\vec{\rho}_\mu-g_\rho\bar{\Psi}_i\gamma^\mu\vec{\rho}_\mu\vec{\tau}\Psi_i\\&-\frac{1}{4}F^{\mu\nu}F_{\mu\nu}-e\bar{\Psi}_i\gamma^\mu\frac{(1-\tau_3)}{2}A_\mu\Psi_i.\end{aligned}\tag{1}$$

The meson fields included are those of the isoscalar σ meson, the isoscalar-vector ω meson, and the isovector-vector ρ meson. The arrows in Eq. (1) denote the isovector quantities. The z component of isospin, τ_3, is taken to be $+1$ for neutrons and -1 for protons. For an appropriate description of

*Electronic address: tapassil@veccal.ernet.in
†Electronic address: bijay@tnp.saha.ernet.in
‡Electronic address: jadu@veccal.ernet.in
§Electronic address: samaddar@tnp.saha.ernet.in

 ©2001 The American Physical Society

the nuclear surface properties [13], a scalar self-interaction term $U(\sigma)$ of the σ meson is included in the Lagrangian,

$$U(\sigma)=\frac{1}{2}m_\sigma^2\sigma^2+\frac{1}{3}g_2\sigma^3+\frac{1}{4}g_3\sigma^4. \tag{2}$$

The quantities M, m_σ, m_ω, and m_ρ are the nucleon, σ-, ω-, and the ρ-meson masses, respectively, while g_σ, g_ω, g_ρ, and $e^2/4\pi=1/137$ are the corresponding coupling constants for the mesons and the photon. The field tensors of the vector mesons and of the electromagnetic fields have the following structure:

$$\Omega^{\mu\nu}=\partial^\mu\omega^\nu-\partial^\nu\omega^\mu, \tag{3}$$

$$\vec{\mathbf{R}}^{\mu\nu}=\partial^\mu\vec{\rho}^\nu-\partial^\nu\vec{\rho}^\mu-g_\rho(\vec{\rho}^\mu\times\vec{\rho}^\nu), \tag{4}$$

$$F^{\mu\nu}=\partial^\mu A^\nu-\partial^\nu A^\mu. \tag{5}$$

The equations of motion are obtained from the variational principle. The mean field approximation is introduced at this stage by treating the fields as c numbers or classical fields. This results in a set of coupled equations, namely, the Dirac equation with potential terms for the nucleons and the Klein-Gordon-type equations with sources for the mesons and the photon. Time reversal invariance and charge conservation simplify the equations in the static case. The resulting equations, known as relativistic mean-field equations, have the following form. The Dirac equation for the nucleon is

$$\{-i\alpha\cdot\nabla+\mathcal{V}(\tau_3,\mathbf{r})+\beta[M+\mathcal{S}(\mathbf{r})]\}\Psi_i=\epsilon_i\Psi_i, \tag{6}$$

where

$$\mathcal{V}(\tau_3,\mathbf{r})=g_\omega\omega_0(\mathbf{r})+g_\rho\tau_3\rho_0(\mathbf{r})+e\frac{(1-\tau_3)}{2}A_0(\mathbf{r}) \tag{7}$$

and

$$\mathcal{S}(\mathbf{r})=g_\sigma\sigma(\mathbf{r}) \tag{8}$$

are the *vector* and the *scalar* potentials, respectively. The *scalar* potential contributes to the effective mass as

$$M^*(\mathbf{r})=M+\mathcal{S}(\mathbf{r}). \tag{9}$$

The Klein-Gordon equations for the mesons and the electromagnetic fields with the nucleon densities as sources are

$$\{-\Delta+m_\sigma^2\}\sigma(\mathbf{r})=-g_\sigma\rho_s(\mathbf{r})-g_2\sigma^2(\mathbf{r})-g_3\sigma^3(\mathbf{r}), \tag{10}$$

$$\{-\Delta+m_\omega^2\}\omega_0(\mathbf{r})=g_\omega\rho_v(\mathbf{r}), \tag{11}$$

$$\{-\Delta+m_\rho^2\}\rho_0(\mathbf{r})=g_\rho\rho_3(\mathbf{r}), \tag{12}$$

$$-\Delta A_0(\mathbf{r})=e\rho_c(\mathbf{r}). \tag{13}$$

While considering a finite nucleus, for simplicity, we assume it to be spherically symmetric. The above field equations then can be written in a general form

$$\left(-\frac{\partial^2}{\partial r^2}-\frac{2}{r}\frac{\partial}{\partial r}+m_\phi^2\right)\phi(r)=S_\phi(r), \tag{14}$$

where m_ϕ are the meson masses for $\phi=\sigma$, ω, and ρ and is zero for the photon. The source term $S_\phi(r)$ is given by the right-hand side of Eqs. (10)–(13) for σ,ω,ρ and Coulomb fields. The above equation (14) can be solved using the Green's function [10]

$$\phi(r)=\int_0^\infty r'^2G_\phi(r,r')S_\phi(r')dr', \tag{15}$$

where

$$G_\phi(r,r')=\frac{1}{2m_\phi rr'}[e^{-m_\phi|r-r'|}-e^{-m_\phi|r+r'|}], \tag{16}$$

for the massive fields, and

$$G_\phi(r,r')=\begin{cases}\dfrac{1}{r} & \text{for } r>r',\\[2ex] \dfrac{1}{r'} & \text{for } r<r',\end{cases} \tag{17}$$

for the Coulomb field.

The quantities ρ_s, ρ_v, ρ_3, and ρ_c appearing on the right-hand side of Eqs. (10)–(13) are the scalar, baryon, isovector, and charge densities, respectively. They can be obtained as

$$\rho_s(r)=\sum_{\tau_3}\rho_s(\tau_3,r),$$

$$\rho_v(r)=\sum_{\tau_3}\rho_v(\tau_3,r),$$

$$\rho_3(r)=\sum_{\tau_3}\tau_3\rho_v(\tau_3,r),$$

$$\rho_c(r)=\sum_{\tau_3}\left(\frac{1-\tau_3}{2}\right)\rho_v(\tau_3,r). \tag{18}$$

In the Thomas-Fermi approximation, the quantities $\rho_v(\tau_3,r)$ and $\rho_s(\tau_3,r)$ are given as

$$\rho_v(\tau_3,r)=\frac{\gamma}{2\pi^2}\int_0^\infty f(\epsilon,T)k^2dk, \tag{19}$$

$$\rho_s(\tau_3,r)=\frac{\gamma}{2\pi^2}\int_0^\infty\frac{M^*(r)}{\sqrt{k^2+M^{*2}(r)}}f(\epsilon,T)k^2dk, \tag{20}$$

where the spin degeneracy factor γ is equal to 2. The self-consistent occupancy function $f(\epsilon,T)$ is obtained through the minimization of the thermodynamic potential

$$G=E-TS-\mu N \tag{21}$$

and is given by

$$f(\epsilon,T)=\frac{1}{1+e^{(\epsilon-\mu)/T}}, \tag{22}$$

with

$$\epsilon(\tau_3,k,r)=\mathcal{V}(\tau_3,r)+\sqrt{k^2+M^{*2}(r)}. \tag{23}$$

The chemical potential μ is adjusted to get the desired number of particles (neutrons and protons) given by

$$n(\tau_3)=4\pi\int_0^{r_{max}} r^2\rho_v(\tau_3,r)dr. \tag{24}$$

In Eq. (24), r_{max} determines the confining volume V taken to be spherical. From Eqs. (19) and (22), it can be seen that at large distances the baryon density $\rho_v \sim e^{(\mu-M)/T}$ and is therefore a nonzero constant at finite temperature. The solution to the baryon density and hence the various observables depends on the choice of the size of the box in which the calculation is performed. At zero temperature, however, the solution is independent of the choice of the confining volume once it is larger than the normal nuclear volume V_0. Exactly the same characteristic is seen in the nonrelativistic case [14,15]. The choice of the volume for the evaluation of the thermodynamic variables will be discussed in the next section.

For a nuclear system with mass number A, the total energy $E(T)$ is given by [10]

$$E(T)=E_{part}+E_\sigma+E_{\sigma NL}+E_\omega+E_\rho+E_C+E_{\text{c.m.}}-AM, \tag{25}$$

with

$$E_{part}=\frac{2\gamma}{\pi}\sum_{\tau_3}\int_0^{r_{max}} r^2dr\int_0^\infty k^2\epsilon(\tau_3,k,r)f(\epsilon,T)dk, \tag{26}$$

$$E_\sigma=-\frac{1}{2}g_\sigma\int d^3r\rho_s(\mathbf{r})\sigma(\mathbf{r}), \tag{27}$$

$$E_{\sigma NL}=-\frac{1}{2}\int d^3r\left\{\frac{1}{3}g_2\sigma^3(\mathbf{r})+\frac{1}{2}g_3\sigma^4(\mathbf{r})\right\}, \tag{28}$$

$$E_\omega=-\frac{1}{2}g_\omega\int d^3r\rho_v(\mathbf{r})\omega^0(\mathbf{r}), \tag{29}$$

$$E_\rho=-\frac{1}{2}g_\rho\int d^3r\rho_3(\mathbf{r})\rho^0(\mathbf{r}), \tag{30}$$

$$E_C=-\frac{e^2}{8\pi}\int d^3r\rho_C(\mathbf{r})A^0(\mathbf{r}), \tag{31}$$

$$E_{\text{c.m.}}=-\frac{3}{4}\hbar\omega_0=-\frac{3}{4}41A^{-1/3}. \tag{32}$$

The free energy F is given by $(E-TS)$ where the entropy S can be calculated from the Landau quasiparticle approximation,

$$S=-\frac{2\gamma}{\pi}\sum_{\tau_3}\int_0^{r_{max}} r^2dr\int_0^\infty k^2[flnf+(1-f)ln(1-f)]dk. \tag{33}$$

The specific heat C_v and the pressure P can be calculated from

$$C_v=\left.\frac{dE}{dT}\right|_V, \tag{34}$$

$$P=-\left.\frac{dF}{dV}\right|_T. \tag{35}$$

The baryonic density and the mesonic and Coulomb fields are obtained iteratively through the following scheme.

(i) An initial guess is made for the fields $\sigma(r)$, $\omega(r)$, $\rho(r)$, and $A_0(r)$.

(ii) The effective mass M^* and the energy ϵ given by Eqs. (9) and (23), respectively, are calculated with the guessed fields. The proton and neutron chemical potentials (μ) are adjusted to reproduce the given number of nucleons of each kind.

(iii) From Eq. (18), the various densities and hence the source terms are calculated.

(iv) These source terms are used in Eqs. (10)–(13) for the generation of the new fields.

Steps (ii)–(iv) are repeated until the desired accuracy is reached.

The expressions for the EOS for nuclear matter can be obtained as a special case of a finite nucleus by ignoring the gradient terms in the field equations. This simplifies the expressions for the relevant observables and are given in Ref. [6].

III. RESULTS AND DISCUSSIONS

In this section, the results of our calculations for the EOS of infinite symmetric and asymmetric nuclear matter as well as of a few finite nuclear systems are first given. We have chosen ^{40}Ca, ^{109}Ag, and ^{150}Sm as the reprersentative systems. The results of our calculations of the caloric curve for these nuclei are next presented. A host of parameter sets for the nonlinear σ-ω-ρ model are available which produce almost similar ground state properties of nuclei over the whole periodic table but with widely different values of nuclear incompressibility (K_∞). To study the effects of different K_∞ on the results of our calculations, we have chosen the parameter sets NL1, NL3, and NLSH [10,16], having K_∞ equal to 212, 272, and 356 MeV, respectively.

A. Nuclear EOS

The EOS of symmetric and asymmetric nuclear matter in the RTF theory has already been calculated by Müller and Serot [7]. For comparison of results for finite nuclei obtained

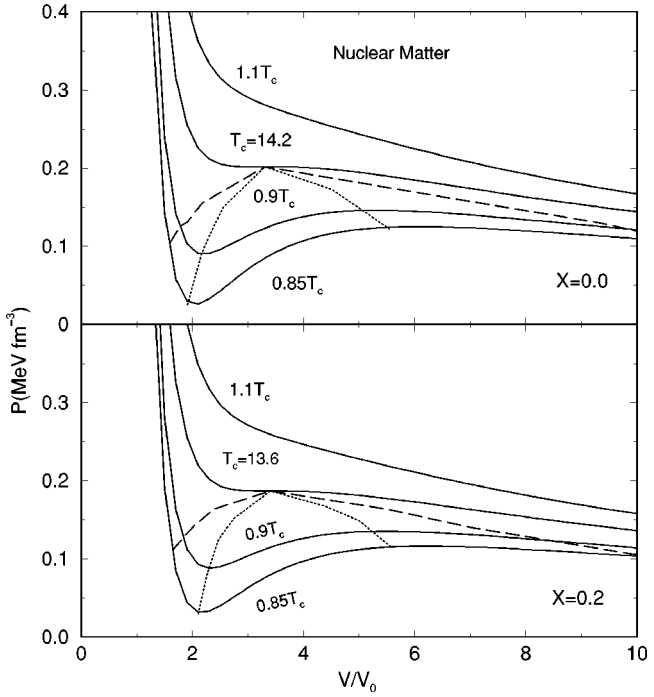

FIG. 1. The equation of state for symmetric nuclear matter (top panel) and of asymmetric nuclear matter (bottom panel) with NL3 parameter set. The temperatures (in MeV) for the isotherms are as marked in the figure. The dotted lines are the spinodals and the dashed lines are the coexistence curves.

with a given set of parameters and also for completeness, we have repeated the calculations for infinite systems with the same given parameter set. In Fig. 1, the isotherms of symmetric nuclear matter (top panel) and asymmetric nuclear matter (bottom panel) with $X=0.2$ are displayed. The asymmetry parameter is defined as $X=(\rho_n-\rho_p)/(\rho_n+\rho_p)$. The abscissa refers to ρ_0/ρ $(=V/V_0)$ where ρ_0 is the saturation density of normal nuclear matter given by 0.15 fm^{-3}. The isotherms are calculated with the NL3 parameter set and are shown for a few temperatures, at and around the critical temperature T_c. For symmetric matter, T_c is 14.2 MeV, whereas for the asymmetric matter considered, it is 13.6 MeV. The isotherms resemble closely those obtained for the van der Waals systems and are not quantitatively very different from those found in the nonrelativistic approach [8]. The dashed and dotted lines in the figure are the liquid-gas coexistence line and the spinodal line, respectively. With the other parameter sets, the results are very similar; however, the critical temperature is found to increase and the critical volume becomes smaller for the parameter set which gives larger incompressibility. The critical temperature and the critical volume for the different parameter sets are given in Table I.

For the symmetric infinite system, the liquid-gas coexistence line is obtained from the Maxwell construction as it is effectively a one-component system. Here the pressure and the chemical potential in the two phases are the same at a fixed temperature (Gibbs criteria) throughout their coexistence for any value of λ where λ is the liquid volume fraction (the gas volume fraction is $1-\lambda$). Then the neutron-proton asymmetry is zero in both phases for all values of λ. The asymmetric nuclear matter is a two-component system; here, for any λ, not only do the Gibbs criteria need to be fulfilled for the thermodynamical coexistence of the liquid and gas phases, the overall asymmetry (neutron-proton ratio) has to be conserved which introduces added complications. Now, the pressure, chemical potentials, and the neutron-proton ratio in both phases are in general changing functions of the volume fraction [7]. We have taken these factors into account to determine the liquid-gas coexistence region. The spinodals shown in Fig. 1 are the isothermal spinodals referring to mechanical instability. The diffusive spinodal [17] for the asymmetric matter is not shown here.

Finite nuclei (even symmetric ones) with the Coulomb interaction switched on behave like two-component systems. However, the ideas expounded earlier for asymmetric nuclear matter for the construction of the liquid-gas coexistence lines cannot be employed to the case of finite systems. The density in finite nuclei is not uniform unlike infinite nuclear matter which is homogeneous in either the liquid or gas phase. For an asymmetric infinite system, we have found that for liquid-gas coexistence, in general, the neutron-proton ratio in the gas phase is much larger than that in the liquid phase. There is thus a phase separation between the neutrons and protons. For the construction of the isotherms for finite nuclei, the system is enclosed in a finite volume; then the self-consistent solution of the density profiles does not allow any significant neutron-proton phase separation because of the strong attractive unlike pair interactions compared to the interaction among like pairs. Indeed, from numerical calcu-

TABLE I. Critical temperature and critical volume for a few systems in the RTF model with parameter sets NL1, NL3, and NLSH, and in the NRTF model with the SBM interaction.

Systems	T_c (MeV)				V_c/V_0			
	NL1	NL3	NLSH	SBM	NL1	NL3	NLSH	SBM
Sym. NM	13.4	14.2	15.4	14.5	3.9	3.3	2.9	2.8
Asy. NM ($X=0.2$)	12.7	13.6	14.7	14.1	4.1	3.4	3.0	2.9
^{40}Ca	11.1	11.6	12.4	–	6.7	6.5	5.8	–
^{150}Sm (with Coulomb interaction)	11.4	12.0	13.0	11.8	5.4	5.0	4.4	4.9
^{150}Sm (no Coulomb interaction)	12.3	12.9	14.0	12.5	6.4	6.0	5.2	6.2

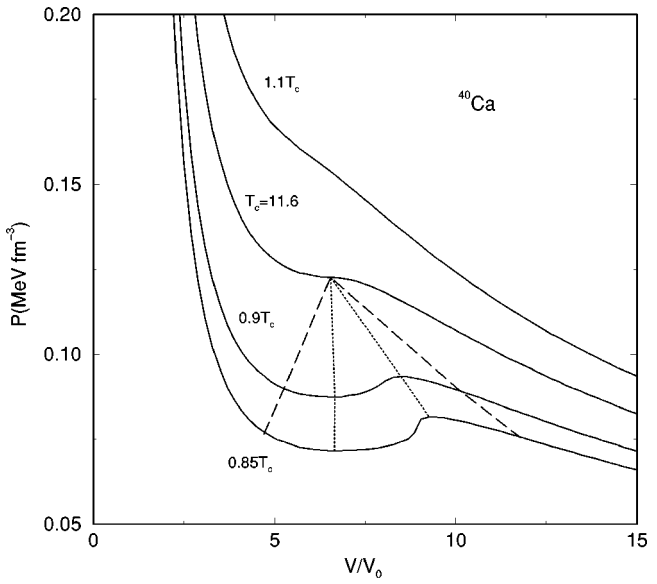

FIG. 2. The equation of state for the nucleus ^{40}Ca for the NL3 parameter set. The different notations used have the same meaning as in Fig. 1.

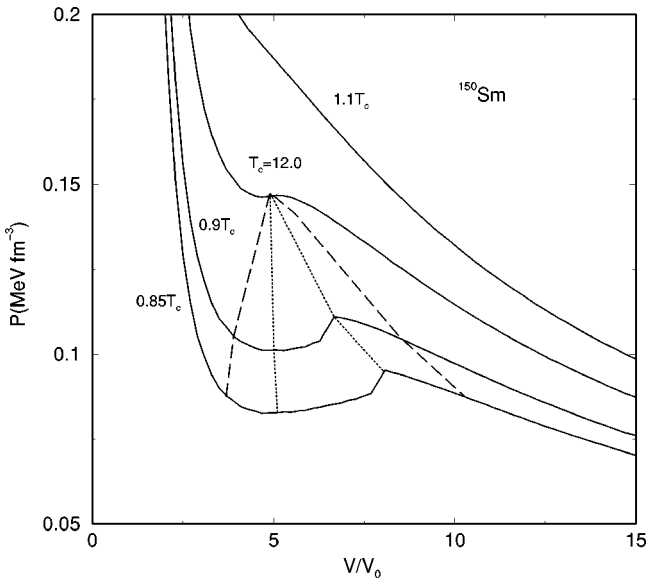

FIG. 3. Same as in Fig. 2 but for the nucleus ^{150}Sm.

lations, we find that the N/Z ratio throughout the nuclear volume is nearly the same (not varying by more than 10%) at all temperatures beyond $T\sim 3.0$ MeV. For a two-component thermodynamic system, liquid-gas coexistence occurs along the Maxwell line (constant pressure, equal areas in the unstable phases in the P-V diagram) if the ratios of the concentrations of the components are the same in the two phases, as it is then effectively a one-component system. It is known that for small finite one-component systems, the pressure in the coexistence region may have a small negative slope [18] in the P-V plane, but for symmetric nuclei with the Coulomb interaction switched off, we find numerically that the conventional Maxwell construction is an excellent approximation as the differences in the chemical potentials on both ends of the Maxwell line are negligibly small. It is found that for the asymmetric finite nuclei under study (even with the Coulomb interaction on), the difference in the neutron or the proton chemical potentials at the ends of the Maxwell line is typically ~ 0.2 MeV only, which is around 30–40 times smaller compared to that for infinite nuclear matter with the same asymmetry. We therefore expect that for these finite systems, for the determination of the liquid-gas coexistence, a conventional Maxwell construction may not be a poor approximation to which we have resorted to in the present calculations for the nuclei considered.

The isotherms for the lightest nucleus ^{40}Ca and the heaviest nucleus ^{150}Sm that we consider are shown in Figs. 2 and 3, respectively, for the parameter set NL3. The results with the other parameter sets are not displayed as they look very similar. The finite size effects and the Coulomb interactions between protons do not change the qualitative character of the isotherms; the only effects are the lowering of the critical temperature and raising of the critical volume to some extent. The coexistence lines and the isothermal spinodal lines are shown by the dashed and dotted lines, respectively. The critical temperatures and the critical volumes for different parameter sets are shown in Table I. The finite size effects as well as the Coulomb interaction tend to reduce the critical temperature. To isolate the Coulomb effect, the critical parameters for ^{150}Sm are also displayed in Table I switching off the Coulomb interaction. It is seen that the Coulomb interaction lowers T_c for ^{150}Sm by about 1 MeV. The nature of the EOS shows that it is possible to have a liquid-gas phase transition in a finite nuclear system below the critical temperature T_c if it is prepared suitably in thermodynamic equilibrium.

To make a quantitative comparison of the results in the RTF theory with those obtained in the nonrelativistic Thomas-Fermi (NRTF) framework [8], the NRTF results for the critical temperatures and the critical volumes for nuclear matter and for the nucleus ^{150}Sm are also given in Table I. The NRTF calculations were performed with a modified Seyler-Blanchard (SBM) effective interaction which gives $K_\infty \approx 240$ MeV. This lies in between those obtained with NL1 and NL3 parameter sets. However, it is seen that the critical parameters for the SBM calculations are in between NL3 and NLSH for infinite nuclear matter and close to those obtained with the NL3 parameter set for finite systems. The nature of the EOS and critical parameters is controlled by the single-particle potential and the effective mass. To compare these quantities in the RTF and in the NRTF models, we display in Fig. 4 the nucleon single-particle potential as a function of the nuclear density (scaled with the normal nuclear density ρ_0) for symmetric nuclear matter as given in the two models. The single-particle potential in the RTF is taken to be $\mathcal{V}+\mathcal{S}$ as given by Eqs. (7) and (8). The corresponding effective masses are shown in Fig. 5. It is seen that the SBM single-particle potential is very close to that obtained with the NL1 parameter set at lower densities which evolves towards that generated with the NL3 parameter set with increasing density. The effective mass in the NRTF model is only a few percent lower at low densities and near the normal nuclear matter density it becomes somewhat higher compared to those obtained in the RTF model. The

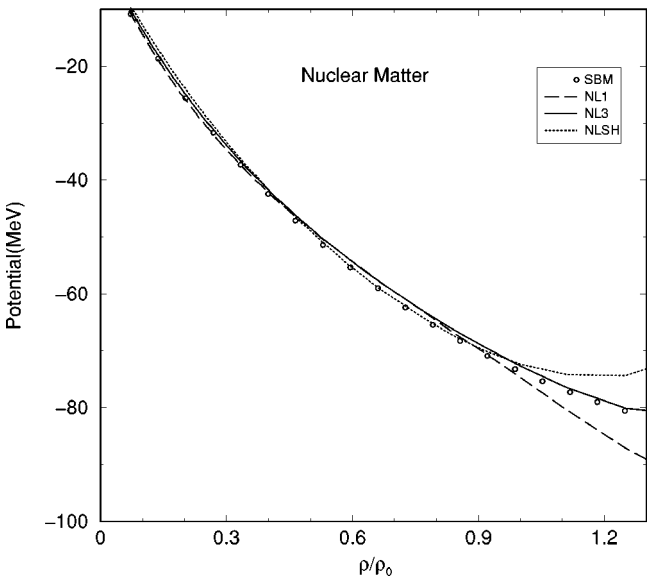

FIG. 4. Plot for the relativistic and nonrelativistic mean field potentials as a function of density for symmetric nuclear matter at zero temperature.

single-particle potentials for protons as a function of distance from the center of the nucleus (^{150}Sm) in the two models corresponding to the ground state and at a temperature $T=8$ MeV are shown in the top and bottom panels of Fig. 6, respectively. The neutron single-particle potentials (not shown) have very similar behavior. It is seen that the potentials obtained in the NRTF model and those obtained with the different parameter sets in the RTF models are quite close. The effective mass for finite nuclei in the two models is consistent with that shown in Fig. 5; i.e., the NRTF model yields an effective mass which is a little higher at the center and lower at the surface compared to the RTF ones. The

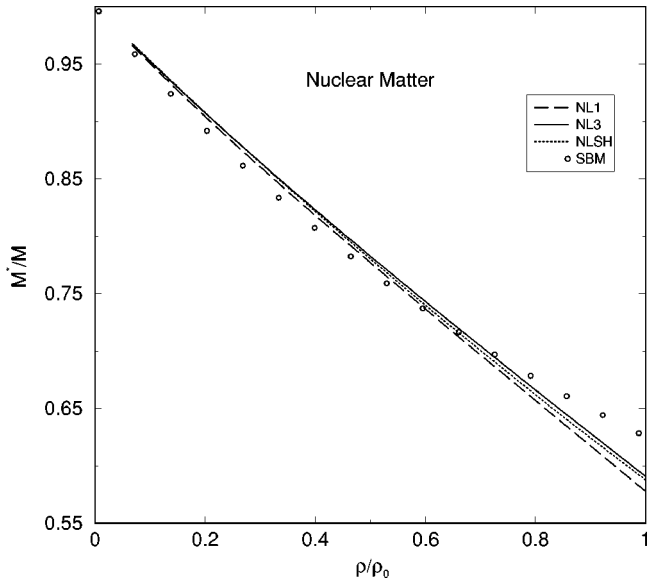

FIG. 5. Density dependence of nucleon effective mass for symmetric nuclear matter at zero temperature calculated within the relativistic and nonrelativistic frameworks.

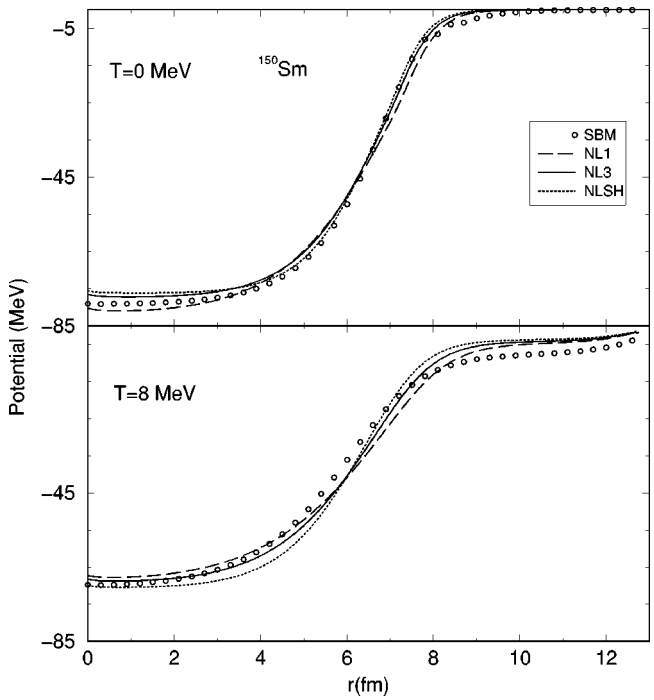

FIG. 6. Relativistic and nonrelativistic mean field potentials for protons at temperatures $T=0$ MeV (top panel) and $T=8$ MeV (bottom panel) for the nucleus ^{150}Sm.

above results clearly demonstrate the closeness of the single-particle potential and the effective mass in the nonrelativistic and relativistic frameworks. So it is natural to expect that the EOS and the related thermodynamic properties would not be very different.

B. Caloric curve

We have remarked before that the density and hence the observables depend on the volume in which the nucleus at finite temperature is confined. The calculation of the excitation energy as a function of temperature (the caloric curve) is thus volume dependent. In the experimental situation with energetic heavy ion collisions, it is generally assumed that the hot nuclear system prepared after the collision expands substantially beyond its normal size ($\sim 4-8$ times V_0) and then undergoes fragmentation due to density instabilities. Guided by the practice that many theoretical calculations for heavy ion collisions are done by imposing that thermalization occurs in a freeze-out volume, we fix a volume and then find the caloric curve. The freeze-out volume V is determined by r_{max} occurring in Eqs. (26)–(33) as $V/V_0=(1/A)\times(r_{max}/r_0)^3$. Here r_0 is the radius parameter corresponding to the normal nuclear volume V_0; it is taken to be 1.2 fm.

In order to see the signature of liquid-gas phase transition, it is evident that the freeze-out volume is to be chosen beyond the critical volume V_c. It is seen from Table I that for the nuclei considered, $V_c \sim 5-6$ times V_0. We have fixed the freeze-out volume as $8V_0$ for our calculations. In Fig. 7, the caloric curves for the nuclei ^{40}Ca, ^{109}Ag, and ^{150}Sm are displayed with the three different parameter sets. The caloric curves are seen to be nearly independent of the parameter

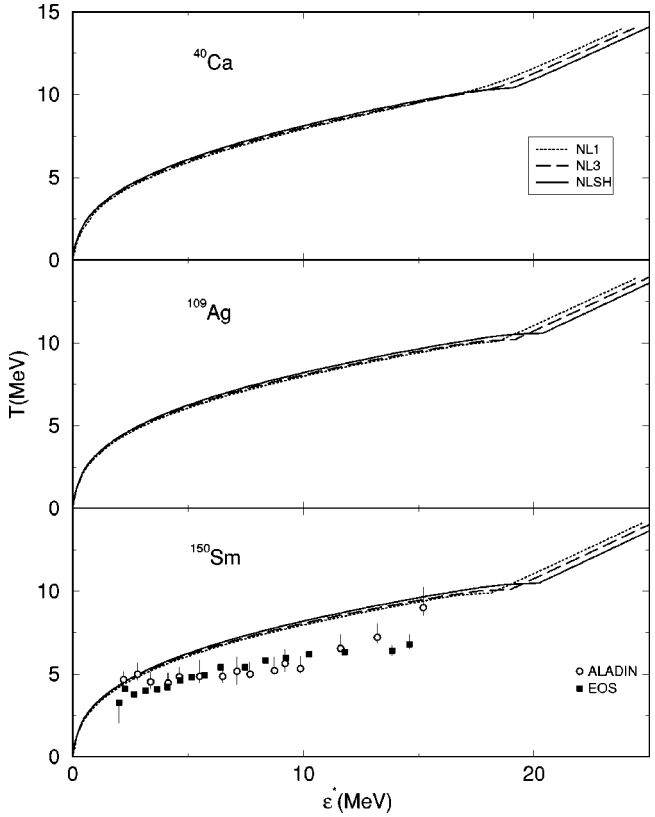

FIG. 7. Caloric curves for the systems ^{40}Ca, ^{109}Ag, and ^{150}Sm. Open circles and solid squares in the bottom panel represent the experimental data for ALADIN and EOS Collaborations.

sets. At lower temperatures, the excitation energy per particle ϵ^* increases quadratically with temperature similar to that in a Fermi gas; for T between 5 and 10 MeV, the caloric curve exhibits a shoulder and beyond that with a kink ϵ^* rises linearly with temperature as observed for a classical gas. In the bottom panel of Fig. 7 the data for experimental caloric curves for the ALADIN and EOS Collaborations are also shown. It is noted that the calculated caloric curves show shoulders at temperatures significantly higher than those obtained from experiments. This may be attributed to (i) the neglect of fluctuations in the theory which is expected to play important role near the transition temperature and (ii) the neglect of collective flow which lowers the transition temperature appreciably as seen in the nonrelativistic calculations [8]. The specific heat C_v defined by Eq. (34) for the three parameter sets is shown in Figs. 8 and 9 for the three systems studied. Except for the top panel in Fig. 8, the calculations reported are done at the freeze-out volume $8V_0$. The heat capacity shows a sharp peak, signaling the liquid-gas phase transition, the peaks occurring at those temperatures where the caloric curve exhibits a kink. It is found that the harder the EOS, the larger the transition temperature (T_p) and the sharper the peak. In the top panel of Fig. 8, the specific heat for ^{40}Ca with a freeze-out volume $4V_0$ is displayed. Instead of a sharp peak, it shows a broad bump at $T\sim 10$ MeV. Here the freeze-out volume is less than the critical volume. We do not associate this bump with a liquid-gas phase transition; it possibly signals a precursor to the transition.

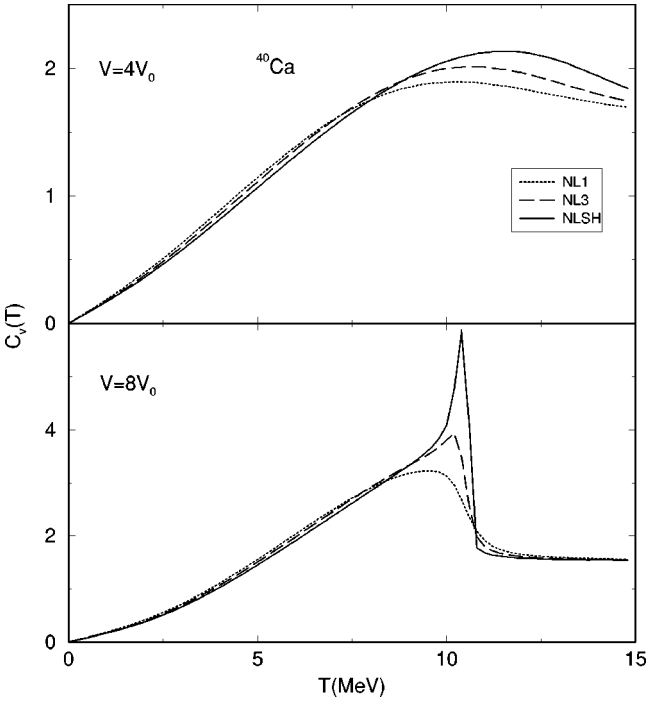

FIG. 8. The specific heat for ^{40}Ca at freeze-out volume equal to $4V_0$ (upper panel) and $8V_0$ (lower panel) with different parameter sets as labeled.

The evolution of the density distributions for the three systems around the phase transition temperature T_p is dis-

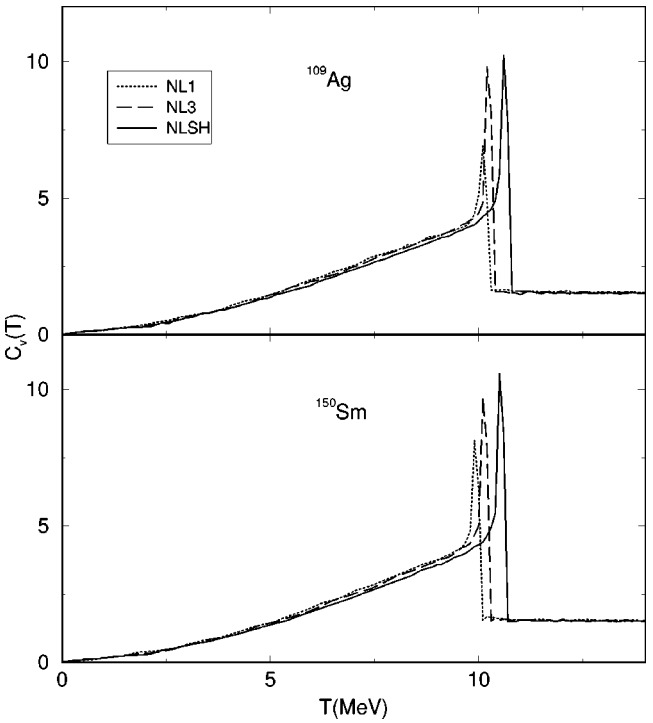

FIG. 9. The specific heat for the nucleus ^{109}Ag (upper panel) and ^{150}Sm (lower panel) at the freeze-out volume $8V_0$ with different parameter sets.

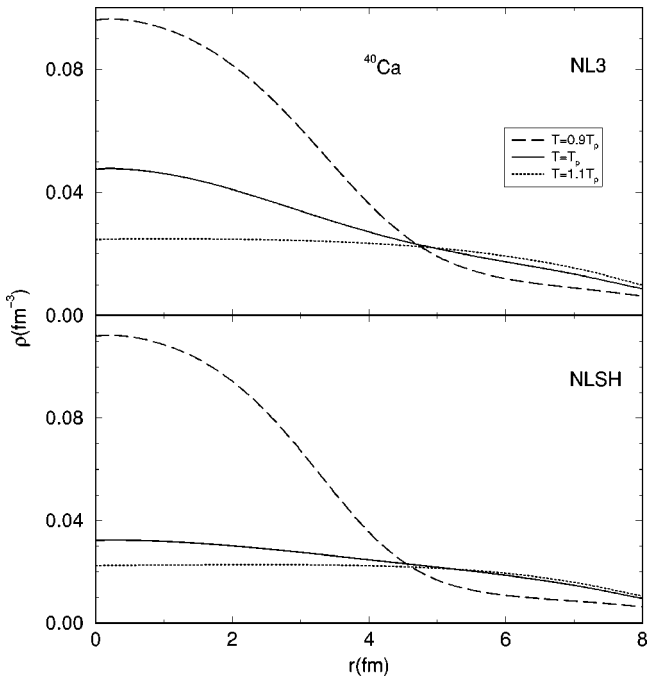

FIG. 10. Density distributions around transition temperatures $T_p = 10.1$ and 10.3 MeV at a freeze-out volume $8V_0$ for ^{40}Ca with parameter sets NL3 (upper panel) and NLSH (lower panel), respectively.

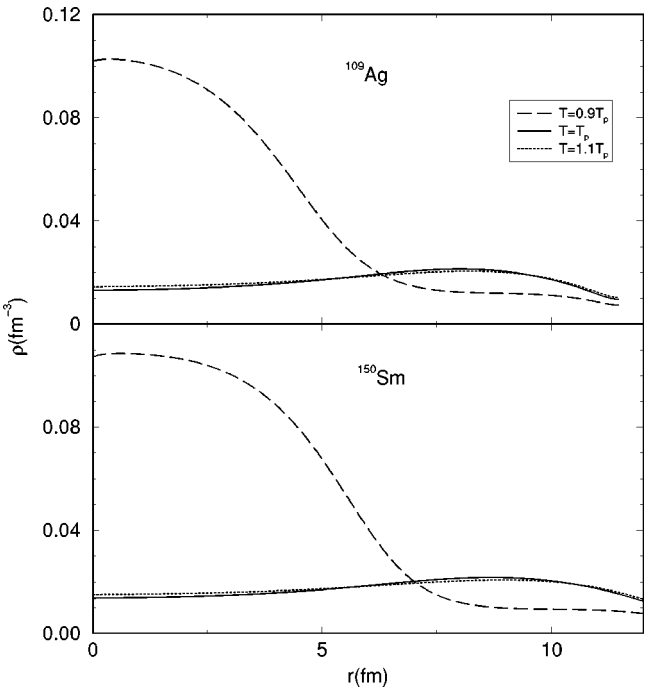

FIG. 11. Density distribution around the transition temperatures $T_p = 10.2$ and 10.3 MeV for ^{109}Ag (upper panel) and ^{150}Sm (lower panel), respectively, with NL3 parameter set at a freeze-out volume $8V_0$.

played in Figs. 10 and 11. The calculations are done in a freeze-out volume $8V_0$. In Fig. 10, the density distribution for ^{40}Ca with the parameter sets NL3 (top panel) and NLSH (bottom panel) is shown. At low temperatures, the density is more like a Woods-Saxon profile; with increasing temperature, the central density depletes and a long tail spreading to the boundary develops as is shown by the dashed line at $T = 0.9T_p$. With further increase in temperature to T_p and a little beyond, the density distribution tends to be uniform as is evident from the solid line ($T = T_p$) and the dotted line ($T = 1.1T_p$). It is found that the evolution of density with temperature is nearly independent of the parameter sets and therefore for the nuclei ^{109}Ag and ^{150}Sm calculations with only NL3 parameter sets are shown in Fig. 11. For these nuclei too the evolution of density is very similar to that in ^{40}Ca. The rapid change in the density distribution towards a uniform one as the temperature approaches T_p is a further indication of a liquid-gas phase transition in these finite systems.

For symmetric nuclear matter, at a fixed temperature, the pressure remains constant over the whole coexistence region. The Gibbs free energy per particle g then shows a kink at the transition temperature when the pressure is held constant. Its derivative with respect to temperature, the entropy function, then shows a discontinuity there. For asymmetric nuclear matter, it has been shown in Ref. [7] that the liquid-gas phase transition is second order, the continuous transition becoming more conspicuous with increasing asymmetry. There the pressure is not constant but shows a negative slope in the coexistence region for an isotherm in the P-V plane. Thus, at constant pressure, the end points of the coexistence line are at different temperatures; then the kink in the Gibbs free energy g disappears and the entropy function becomes continuous with kinks at the end points of the transition. The liquid-gas phase transition thus occurs over a finite temperature interval. For finite nuclei, the exact calculation of the thermodynamic functions in the coexistence region is nontrivial and still not known, but as explained earlier in the

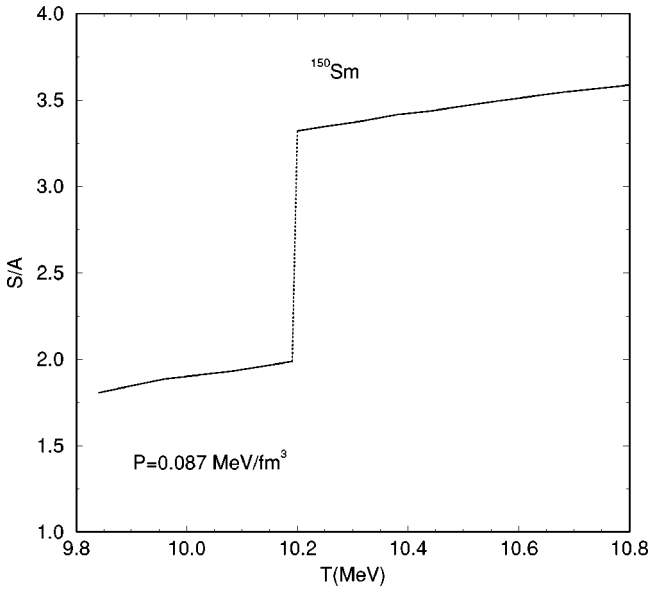

FIG. 12. The temperature evolution of entropy per particle for the system ^{150}Sm at a constant pressure ($P = 0.087$ MeV/fm^3). The dashed line shows the discontinuity at the transition temperature.

beginning of this section, we expect the pressure in this region to remain close to a constant; it is then obvious that the entropy at constant pressure would show a discontinuity at a transition temperature as shown in Fig. 12 indicating a first-order phase transition. A precise statement about the order of the phase transition in finite nuclei can be made only if exact calculations of the partition functions and hence the thermodynamic variables are rendered posssible. The present mean-field theory shows that the liquid-gas phase transition in finite nuclei has characteristics closer to a first-order transition. This is in consonance with the results obtained in the lattice gas model [19]. No definite conclusion can, however, be reached from the experimental data; the GSI data [1] indicate a first-order phase transition whereas the analyses of the EOS data [20] show that the transition may be second order.

IV. CONCLUSIONS

The relativistic mean-field theory which has been very successful in describing the ground state properties of nuclear systems has been applied for the first time in evaluating the equation of state of finite nuclei in this paper. We have resorted to a relativistic self-consistent Thomas-Fermi theory with the nonlinear σ-ω-ρ version of the Lagrangian. It is found that the results do not differ qualitatively from those obtained in a nonrelativistic approach. This is due to the fact that the single-particle potential and the effective mass which control the relevant observables are very similar. The calculations have been done with three parameter sets with very different nuclear incompressibilities; still the EOS look nearly the same and the critical parameters are not too different. The critical parameters for finite nuclei are appreciably different from those of the infinite system. The specific heat C_v calculated from the caloric curve shows peaked structures, signaling a liquid-gas phase transition in the nuclei studied. The near uniformity of the density distribution as the system approaches the transition temperature confirms this further. Analysis of the thermodynamical quantities indicates that this liquid-gas phase transition in the finite nuclei is more compatible with a first-order one.

[1] J. Pochodzalla *et al.*, Phys. Rev. Lett. **75**, 1040 (1995).
[2] J. Hauger *et al.*, Phys. Rev. Lett. **77**, 235 (1996).
[3] J. Cibor *et al.*, Phys. Lett. B **473**, 29 (2000).
[4] H. Jaqaman, A. Z. Mekjian, and L. Zamick, Phys. Rev. C **27**, 2782 (1983); **29**, 2067 (1984).
[5] D. Bandyopadhyay, C. Samanta, S. K. Samaddar, and J. N. De, Nucl. Phys. **A511**, 1 (1990).
[6] B. D. Serot and J. D. Walecka, Adv. Nucl. Phys. **16**, 1 (1986).
[7] H. Müller and B. D. Serot, Phys. Rev. C **52**, 2072 (1995).
[8] J. N. De, B. K. Agrawal, and S. K. Samaddar, Phys. Rev. C **59**, R1 (1999).
[9] J. N. De, S. Dasgupta, S. Shlomo, and S. K. Samaddar, Phys. Rev. C **55**, R1641 (1997).
[10] Y. K. Gambhir, P. Ring, and A. Thimet, Ann. Phys. (N.Y.) **198**, 132 (1990).
[11] G. A. Lalazissis, D. Vretenar, W. Poeschl, and P. Ring, Nucl. Phys. **A632**, 363 (1998).
[12] D. Vretenar, G. A. Lalazissis, and P. Ring, Phys. Rev. Lett. **82**, 4595 (1999).
[13] J. Boguta and A. R. Bodmer, Nucl. Phys. **A292**, 413 (1977).
[14] M. Brack, C. Guet, and H. B. Hakansson, Phys. Rep. **123**, 275 (1985).
[15] J. N. De, N. Rudra, Subrata Pal, and S. K. Samaddar, Phys. Rev. C **53**, 780 (1996).
[16] G. A. Lalazissis, J. Kȯnig, and P. Ring, Phys. Rev. C **55**, 540 (1997).
[17] M. Barranco and J. R. Buchler, Phys. Rev. C **22**, 1729 (1980).
[18] R. K. Pathria, *Statistical Mechanics* (Pergamon, New York, 1985), p. 377.
[19] J. Pan, S. Dasgupta, and M. Grant, Phys. Rev. Lett. **80**, 1182 (1998).
[20] J. B. Elliot *et al.*, Phys. Lett. B **381**, 35 (1996).